










RESEARCH ARTICLE | MAY 10 2024

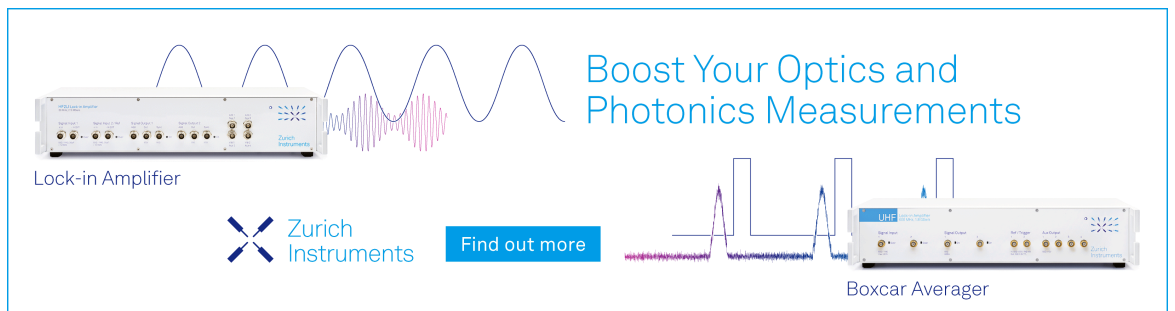
MoLDSTRUCT: Modeling the dynamics and structure of matter exposed to ultrafast x-ray lasers with hybrid collisional-radiative/molecular dynamics

Ibrahim Dawod ; Sebastian Cardoch ; Tomas André ; Emiliano De Santis ; Juncheng E ; Adrian P. Mancuso ; Carl Caleman ; Nicusor Timneanu  




J. Chem. Phys. 160, 184112 (2024)

<https://doi.org/10.1063/5.0197225>



Boost Your Optics and Photonics Measurements

Lock-in Amplifier

 Zurich Instruments

[Find out more](#)

Boxcar Averager

MOLDSTRUCT: Modeling the dynamics and structure of matter exposed to ultrafast x-ray lasers with hybrid collisional-radiative/molecular dynamics

Cite as: J. Chem. Phys. 160, 184112 (2024); doi: 10.1063/5.0197225

Submitted: 12 January 2024 • Accepted: 24 April 2024 •

Published Online: 10 May 2024



View Online



Export Citation



CrossMark

Ibrahim Dawod,^{1,2,a)} Sebastian Cardoch,¹ Tomas André,¹ Emiliano De Santis,³ Juncheng E,²
Adrian P. Mancuso,^{2,4,5} Carl Caleman,^{1,6,b)} and Nicusor Timneanu^{1,c)}

AFFILIATIONS

¹ Department of Physics and Astronomy, Uppsala University, Box 516, SE-75120 Uppsala, Sweden

² European XFEL, Holzkoppel 4, DE-22869 Schenefeld, Germany

³ Department of Chemistry–BMC, Uppsala University, Box 576, SE-75123 Uppsala, Sweden

⁴ Department of Chemistry and Physics, La Trobe Institute for Molecular Science, La Trobe University, Melbourne, Victoria 3086, Australia

⁵ Diamond Light Source, Harwell Science and Innovation Campus, Didcot OX11 0DE, United Kingdom

⁶ Center for Free-Electron Laser Science, Deutsches Elektronen-Synchrotron, Notkestraße 85, DE-22607 Hamburg, Germany

^{a)} Electronic mail: ibrahim.dawod@physics.uu.se

^{b)} Electronic mail: carl.caleman@physics.uu.se

^{c)} Author to whom correspondence should be addressed: nicusor.timneanu@physics.uu.se

ABSTRACT

We describe a method to compute photon–matter interaction and atomic dynamics with x-ray lasers using a hybrid code based on classical molecular dynamics and collisional-radiative calculations. The forces between the atoms are dynamically determined based on changes to their electronic occupations and the formation of a free electron cloud created from the irradiation of photons in the x-ray spectrum. The rapid transition from neutral solid matter to dense plasma phase allows the use of screened potentials, reducing the number of non-bonded interactions. In combination with parallelization through domain decomposition, the hybrid code handles large-scale molecular dynamics and ionization. This method is applicable for large enough samples (solids, liquids, proteins, viruses, atomic clusters, and crystals) that, when exposed to an x-ray laser pulse, turn into a plasma in the first few femtoseconds of the interaction. We present four examples demonstrating the applicability of the method. We investigate the non-thermal heating and scattering of bulk water and damage-induced dynamics of a protein crystal using an x-ray pump–probe scheme. In both cases, we compare to the experimental data. For single particle imaging, we simulate the ultrafast dynamics of a methane cluster exposed to a femtosecond x-ray laser. In the context of coherent diffractive imaging, we study the fragmentation as given by an x-ray pump–probe setup to understand the evolution of radiation damage in the time range of hundreds of femtoseconds.

© 2024 Author(s). All article content, except where otherwise noted, is licensed under a Creative Commons Attribution (CC BY) license (<https://creativecommons.org/licenses/by/4.0/>). <https://doi.org/10.1063/5.0197225>

I. INTRODUCTION

Established x-ray methods help deepen our understanding of how biological systems, such as proteins, viruses, and cells function by providing a three-dimensional view of their structure. For many

decades, synchrotron facilities have been the primary x-ray source for the structure determination of crystallized biomolecules.¹ For non-crystalline samples, cryogenic electron microscopy has emerged as an important imaging tool.² These methods achieve atomic resolution structures but are unable to resolve dynamics on the picosec-

ond to femtosecond time scales.³ X-ray free-electron lasers (XFELs), which provide high repetition intense femtosecond duration x-ray pulses,⁴ have recently been able to follow femtosecond dynamics with atomic resolution.^{5,6}

The appreciable energy deposited in the sample by the x-ray pulses from XFELs leads to measurable structural changes. Depending on the incident beam parameters and characteristics of the sample, structural information can be obtained through coherent diffraction with minimal structural alteration.⁷ Atomic displacement during the pulse is overcome by using shorter pulses than the typical time scales for atomic movement.⁷ Collisional processes from photoelectrons and secondary electrons can lead to further ionization; however, these can also be avoided by pulses of few femtoseconds.^{8,9}

Recent studies have shown that pulses longer than few femtoseconds can be used for imaging due to a self-gating effect where the coherent signal from the later part of the pulse does not contribute with structural information. This is true when imaging single molecules with single particle imaging¹⁰ (SPI) and for protein crystals in serial femtosecond crystallography¹¹ (SFX). In SPI, where only a single copy of the sample is in the interaction region, the recorded diffraction pattern is sensitive to local changes in the molecule. However, as reconstruction algorithms require averaging over many similar patterns, spatially uncorrelated speckle amplitudes have a reduced effect.¹² For SFX, the effect of damage is less severe since there are a great number of copies of the sample, and non-reproducible motion does not contribute to the Bragg spots. If one wishes to achieve resolutions below 1 Å, which is required to follow detailed electron density changes¹³ in systems such as metalloproteins, the damage needs to be quantified. Even in the case of negligible atomic displacement, it is important to consider non-neutral charge states in the reconstruction process as it could improve molecular model fits. Therefore, one needs a reliable tool to quantify radiation damage given a set of materials and x-ray pulse conditions.

Theoretical studies focused on modeling photon–matter interactions are relevant to assess the limits of an experiment and provide a guide for which parameters to use in order to gain optimal results.⁹ As SPI and SFX methods are continuously developed, there are several emerging methods at XFELs for structural determination, such as fluctuation x-ray scattering¹⁴ and x-ray fluorescence intensity correlations,¹⁵ where the ultrafast dynamics and ionization during the pulse play a significant role. In extreme cases during imaging experiments, the sample reaches a highly energetic and strongly coupled state at solid density, referred to as warm dense matter.¹⁶ The exploration of such unique transient states is now accessible at XFELs, and validation of theoretical models to describe it is needed.

Several different published models are available for calculating radiation doses¹⁷ and modeling photon–matter interaction including atomic dynamics for XFELs.^{18–21} A theoretical model to assess the potential of imaging biomolecules using x-ray lasers was first developed by Neutze *et al.*⁷ They employed molecular dynamics (MD) to study time scales of Coulomb explosions in a protein due to an x-ray laser, based on tabulated cross sections of photoionization and Auger–Meitner lifetimes. The dynamics of the free electrons were not followed as the sample was not considered large enough to trap them. Later work focused on studying

larger systems motivating the development of continuum models, which do not have sample size limitations.⁸ To get detailed information in regards to the atomic dynamics, hybrid schemes were developed to treat ion and electron dynamics on different time scales. These included models where the ions were followed using molecular dynamics and free electrons as a continuum.²² Models that explicitly follow both the ion and electron dynamics with time^{19,20} require short time steps to resolve the fast movement of the electrons, significantly slowing down the simulations and limiting the system sizes that can be studied. Free electron continuum models^{8,21,23,24} do not suffer from the same computational demands. Furthermore, modeling every electron independently introduces a larger amount of two-body Coulomb interactions compared to a continuum treatment, which increases the simulation time considerably.

The molecular dynamics software GROMACS allows advanced model development, as the interaction force fields between atoms used to study biomolecular systems are easily accessible and can be modified to account for a transient plasma environment, such as the ones studied here. This makes it possible to prepare the sample input, run photon–matter calculations, and analyze the output using a single software package. The calculations are accelerated by utilizing parallel computations as described by domain decomposition in GROMACS. Finally, in contrast to the codes that have been published, our developed version of the code is openly available to be used by the community.²⁵

II. METHODS

We have developed a method to study photon–matter interaction based on hybrid classical molecular dynamics (MD) and collisional-radiative (CR) computations, which we called MOLDSTRUCT. In this work, time-evolved charge distributions, ion/electron temperatures, electronic states, and free electron densities are calculated using the CR code CRETIN.²⁶ However, any other code that outputs this information can be used. For propagating the positions of the atoms, we use a modified version of the classical MD program GROMACS version 4.5.²⁷ With this version, vacuum and periodic boundary conditions can run on multiple central processing unit (CPU) cores through domain decomposition.²⁸ The strength of the CR calculations is that we can compute photon–matter interaction for arbitrarily large samples. This is because the code models the system as a continuum, and therefore, it is not computationally limited to the number of particles in the system. By coupling the CR data to the MD code, we can make use of the strength of MD, which gives direct information regarding the atom's position. This provides the possibility to probe local dynamics in the structure, which can be especially important for active or metallic sites in biomolecules. In the results section, we present studies of a single particle (cluster of atoms), a liquid (bulk water), and a protein crystal (lysozyme).

A. Modeling photon–matter interaction based on the collisional-radiative theory

The first step in our approach builds on a code that can provide the required photon–matter data to be coupled to the molecular dynamics simulations, and in this work, we utilize the code CRETIN. It uses a rate-equation model based on atomic data to evolve the

conditions of the material under non-local thermodynamic equilibrium environment. The atomic data include energy levels as well as cross sections for photon- and electron-induced ionization and excitations, Auger–Meitner relaxation, and their inverse processes using the assumption of statistical equilibrium. At each time step, the code couples radiation transport, electronic populations, temperatures, and densities in an iterative manner until reaching a self-consistent solution. The free electrons produced are not allowed to escape. They are thermalized and described by the Maxwell–Boltzmann distribution with a single temperature. The densities are allowed to change with hydrodynamic expansion. The effects of the atomic environment on the electronic structure are included using continuum lowering, as formulated by using the Stewart–Pyatt model.²⁹ The CR code does not include shake-up/shake-off or molecular information. The model also transitions from the extension of the weakly or strongly coupled regime, which matters for the description during the first few femtoseconds following the pulse. For the simulations shown here, we utilize the screened hydrogenic model for the atoms.³⁰

By utilizing an x-ray probe with specified pulse energy, duration, photon energy, and focal spot, we calculate the time-resolved interaction between photons and matter by incorporating a description of the sample, including its mass density and atomic composition (stoichiometry). From the CR simulation, we acquire the time-resolved fraction of each charge state for every atomic species, the free electron density and temperature, atomic number densities, and electron–ion coupling. The ion and electron temperatures (T_{ion} and T_e) in the CR simulations are coupled in a two-temperature model describing their evolution³¹ through an electron–ion coupling γ ,

$$\frac{dT_{ion}}{dt} = \gamma(T_e - T_{ion}). \quad (1)$$

The equilibration time between ions and electrons depends on the sample and pulse parameters used, and it is estimated to be on the order of multiple hundreds of femtoseconds,³² making electron–ion coupling relevant for simulations on these time scales. The effect of the expansion of the sample on the properties of the electronic distribution and the ions is included through hydrodynamic expansion.²⁶ To simulate the atoms' movement, we have adapted the GROMACS code²⁷ such that the charge states of the atoms are set based on the CR data. We assign integer charges to individual atoms in the MD in a stochastic manner. Averaged together, these closely match the charge states from CRETIN. We do not assign electronic states in GROMACS, therefore, making no distinction between valance and core ionization in the interactions. The effect of the free electrons given by the CR calculation in the MD simulation is included through screening of the non-bonded interactions and by electron–ion coupling using Langevin temperature coupling.^{33,34}

The potential used to model the Coulomb interaction will depend on whether the plasma is in the weakly or strongly coupled regime. This is dependent on the relation between the kinetic energy of the particles and the Coulomb potential that they expe-

rience. If the system is in the weakly coupled regime for the low charge density/high temperature case, we assume that the Coulomb potential ϕ_C is much smaller than the ion or electron temperature T , $\phi_C/k_B T \ll 1$, which results in the Debye-screened (D) Coulomb interaction,

$$\phi_D(r_{ij}) = \frac{1}{4\pi\epsilon_0} \frac{q_i q_j}{r_{ij}} \exp\left(\frac{-r_{ij}}{\lambda_D}\right), \quad (2)$$

where q is the charge, ϵ_0 is the vacuum permeability, and r_{ij} is the distance between ions i and j . The Debye length λ_D is formulated using the thermalized electron temperature T_e and free electron density n_e , which are used to calculate the corresponding Debye length, defined as³⁵

$$\lambda_D = \sqrt{\frac{\epsilon_0 k_B T_e}{n_e e^2}}, \quad (3)$$

with e being the elementary charge and k_B the Boltzmann constant. The validity of utilizing the screened Coulomb interaction with the Debye length (λ_D) depends on whether it is much smaller than the size of the system L and if there are enough electrons N in the interval of the Debye length to make the screening statistically significant. Given these two conditions, the screened Coulomb interaction can be used for all length scales only when $\lambda_D \ll L$ and $N \gg 1$.³⁵ For our simulations, the first condition is always fulfilled but not necessarily the latter. For these cases, Stewart and Pyatt²⁹ developed a theory for calculating the lowering of ionization potentials given a system of charged ions and free electrons, which is used for all values of electron temperatures and densities. Alternatively, the non-linear Poisson equation can be solved self-consistently, where the electron gas adapts to the ion charge density²² and provides means for an inhomogeneous electron density. This is important for systems containing heavy atoms, as they attract more electron density compared to lighter atoms, thus leading to a more inhomogeneous density of free electrons. In this work, the CR simulations use the Stewart–Pyatt²⁹ model to compute the lowering of the potentials of the atoms due to the environment. To be consistent with the CR simulations, the Coulomb potential in the MD were developed based on the same principles as the Stewart–Pyatt model. We incorporated a hybrid Coulomb screening potential valid in the strong and weak coupling regime.³⁶

In the strongly coupled regime with high density/low temperature, the ion sphere (IS) model is more physical. The basis of the ion sphere model is that each ion is surrounded by enough bonded and free electrons to keep the neutrality of the ion sphere. Given an atom with net-charge Q and a free electron density n_e , the radius of the sphere is calculated as

$$R = \left(\frac{3Q}{4\pi n_e}\right)^{1/3}. \quad (4)$$

The potential outside the radius R from the ion is zero, while inside different models for the screening potential are used, such as the uniform electron gas model,^{36,37}

$$\phi_{IS}(r) = \frac{Q}{r} - \frac{Q}{2R} \left(3 - \frac{r^2}{R^2} \right). \quad (5)$$

The ion charge, electron density, and temperature of the plasma dictate whether it is more suitable to use the Debye screening or ion-sphere model. These depend on the pulse parameters and the sample. In some cases, the system is in a state between the two extremes. This motivates the use of a hybrid model that incorporates the ion-sphere model for some radius $r < r'$ (strongly coupled regime) and the Debye screening model for $r > r'$ (weakly coupled regime). By matching the ion sphere and the screened Coulomb model at the boundary $r = r'$ and both their first and second derivatives, one can derive the following form of the electrostatic potential,³⁶

$$\begin{aligned} \phi(r) &= \phi_{IS}(r) + \phi_D(r) \\ &= \frac{c_0}{r} + c_1 - c_2 r^2 + \frac{c_3}{r} \exp\left(-\frac{r}{\lambda_D}\right). \end{aligned} \quad (6)$$

The coefficients c_0, c_1, c_2 , and c_3 are given by the boundary conditions and are dependent on the free electron density, temperature, and ion charge. The boundary point r' , where $\phi_{IS}(r') = \phi_D(r')$ is defined as

$$r' = \lambda_D \left[\left(\left(\frac{R}{\lambda_D} \right)^3 + 1 \right)^{1/3} - 1 \right], \quad (7)$$

and is dependent on the Debye screening length λ_D .

By utilizing the form of the electrostatic potential presented in Eq. (6), the interaction will dynamically adapt to the current state of the plasma, encompassing parameters such as ion charge, electron temperature, and density. This feature renders the use of this model suitable for studying any system that undergoes a transition into plasma. As all interactions between the atoms are formulated by electromagnetic force, screening due to free electrons will affect all interactions between two atoms. Therefore, we also modulated

the Lennard-Jones (LJ) interaction according to the Debye length, similar to the Debye model,

$$\phi_{LJ}(r_{ij}) = \left(\frac{c_{12}}{r_{ij}^{12}} - \frac{c_6}{r_{ij}^6} \right) \exp\left(\frac{-r_{ij}}{\lambda_D}\right). \quad (8)$$

In Fig. 1, we compare the hybrid screening potential, Debye screening potential, and classical Coulomb interactions to illustrate the impact of how reduced the screened potentials are compared to the classical Coulomb interaction. Furthermore, we are interested in understanding when the hybrid screening and Debye screening models become equal. We note that for a lower intensity of $10^{18} \text{ W cm}^{-2}$, shown in Fig. 1(a), there is a difference between the hybrid force and the Debye screened model. Both are heavily reduced compared to the case of no screening; however, the Debye model generally screens more compared to the hybrid model. For the higher intensity shown in Fig. 1(b), the difference is reduced. In addition, we note that the transition point $r = r'$ is shifted to higher values favoring the IS model with time for the lower intensity (going from $r' = 0.0816 \text{ nm}$ to $r' = 0.0865 \text{ nm}$), while it does the opposite for higher intensities (going from $r' = 0.0602 \text{ nm}$ to $r' = 0.0235 \text{ nm}$), thus favoring the DS model.

B. Force field modeling

The force fields used in the MD simulations differ depending on the sample studied. For instance, for metal clusters, non-bonded and bonded Morse and angle potentials suffice to describe the dynamics. This is due to the rather isotropic structure of the system, which allows for the use of only spherically symmetric two-body potentials between atoms. For biological macromolecules such as proteins, the structure is more complicated as they contain, in addition to Coulomb and Lennard-Jones, interactions describing bonds, angles, and dihedrals.

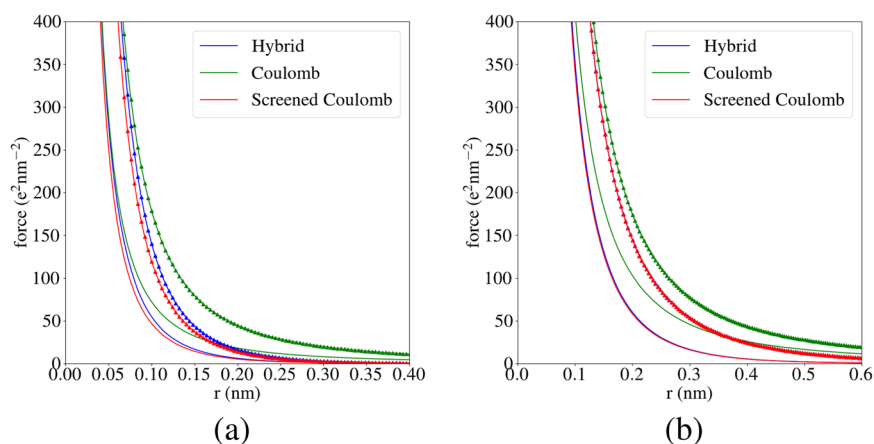


FIG. 1. Electrostatic forces given by the hybrid screening potential in Eq. (6), compared to the Debye Coulomb screening model in Eq. (2) and the unscreened Coulomb force. Data extracted from a simulation of bulk water exposed to a 75 fs flat XFEL pulse with 6860 eV photons and intensity (a) $10^{18} \text{ W cm}^{-2}$ and (b) $5 \times 10^{19} \text{ W cm}^{-2}$. Two time points during the simulation are shown, 10 and 75 fs. The solid lines correspond to the forces after 10 fs, and the solid-dotted lines are the same forces calculated at 75 fs.

The bonded potentials in the force field are valid for the native structure and change during the simulations due to the degree of ionization. Using a scaling factor c , we dynamically modified bonded interactions based on the mean charge \bar{z} of the N -body system, such that

$$c = \begin{cases} 1 - \bar{z}, & \text{for } \bar{z} < 1, \\ 0, & \text{otherwise.} \end{cases} \quad (9)$$

This treatment is supported by the previous density functional theory (DFT) simulations of charged amino acids,³⁸ which show that Coulomb interactions dominate over bonded interactions as charge increases. The motivation for using these potentials even though the sample is defined as plasma is that every atom has a certain probability of being neutral for the entire simulation period. In this case, the bonded terms for these atoms should still remain. For atoms that are bonded in the native structure, we use Morse potentials in order to allow for bond breaking. The potential is defined as

$$V_{\text{Morse}}(r_{ij}) = D_e \exp(-(r_{ij} - b_e)^2), \quad (10)$$

where D_e is the dissociation energy, b_e is the equilibrium distance, and r_{ij} is the current distance of the two i and j atoms involved. For these atom pairs, the LJ interaction is omitted, but we still apply the screened Coulomb interaction. Partial charges present in the native force field are not used since charges are localized to a specific atom when bond breaking occurs.

We omit molecular bonds between atoms that are not initially bonded in the native system. Two charged atoms in a plasma are unlikely to form bonds since the potential energy surface becomes dissociative (i.e., there is no minimum energy) for just a few removed electrons. Thus, the potential energy surface of two arbitrary atoms approaching each other from infinity is best described by a non-bonding potential, such as the LJ interaction. For this potential, the equilibrium distance is usually larger than molecular bond lengths since they are based on the effective ionic radius. This radius decreases as electrons are removed from the atom due to the reduction of the extension of the bound electron cloud. Similar to the previous scaling for bonded interactions, we used a scaling factor $c_{i,j}$ involving pairs of atoms i and j to dynamically modify the LJ potential presented in Eq. (8). The scaling depends on the charge q and atomic number Z of each of the atoms, and is defined as

$$c_{i,j} = \frac{1}{2} \left(\left[1 - \frac{q_i}{Z_i} \right] + \left[1 - \frac{q_j}{Z_j} \right] \right). \quad (11)$$

The scaling factor $c_{i,j}$ has the effect of reducing the constants c_{12} and c_6 and, by extension, altering the equilibrium distance between the two pairs of atoms.

Standard classical MD codes rely on using cutoffs for the non-bonded interactions to reduce the computational time. Since the phase of the matter we probe is pushed into plasma, the cutoff that we use is greatly reduced due to the screening from the free electrons. We compute a suitable non-bonded cutoff by determining the maximum charge states observed in the CR simulations and search for the distance that provides a force smaller than some tolerance. This, in combination with parallelization through domain decomposition, has allowed us to explore large samples on longer time scales.

With all bonded and nonbonded potentials involving interactions between atoms that are defined in the total potential $V(\mathbf{r}) = V_{\text{bonded}}(\mathbf{r}) + V_{\text{nonbonded}}(\mathbf{r})$, we determine the corresponding forces. For propagating the dynamics of the system, we use the leap-frog algorithm in GROMACS to solve Newton's equation,

$$m \frac{d^2 \mathbf{r}_i}{dt^2} = -\nabla V(\mathbf{r}_i), \quad (12)$$

where \mathbf{r}_i is the position of atom i . Equation (12) includes the effect of the free electrons in the screening of the Coulomb interaction between the ions. However, the free electron distribution can also interact with the ions directly, which could affect their trajectories. This is valid for a weakly coupled system where the Coulomb interaction is heavily reduced compared to the kinetic energies. By utilizing the Langevin equation (stochastic dynamics), we introduce two additional terms on the right-hand side of Eq. (12) as

$$m \frac{d^2 \mathbf{r}_i}{dt^2} = -\nabla V(\mathbf{r}) - m_i \gamma \frac{d\mathbf{r}_i}{dt} + \mathbf{f}_i(t), \quad (13)$$

where the first additional term is a friction force. The second additional term is a stochastic Gaussian force^{18,34,39} with the following property for the magnitude $\mathbf{f}_i(t)$,

$$\langle f^i(t) f^i(t + t') \rangle = 2m_i \gamma_i k_B T_e \delta(t'), \quad (14)$$

which means that calculation of the Gaussian force at each time point for atom i is independent of any other time point. The constant γ with unit s^{-1} is calculated using the electron-ion coupling g_{e-ion} from the CR calculation and the number density ρ_N as $\gamma = \rho_N g_{e-ion}$. T_e is the electron temperature retrieved from the CR calculations. The model for the electron-ion coupling parameter g_{e-ion} will dictate the energy transfer between the ions. In our model, we use an average value over time, calculated specifically from the CR simulations for every atomic species, for the coupling parameters as it does not change much during the simulation. The electron temperature is dynamically changed at every time step, and it is read from the CR calculations.

In our model, we are limited by the size of the single particle as the CR code assumes no escaping electrons and we simulate them in vacuum. We estimated the minimum size of a single particle based on the pulse parameters used to trap all produced free electrons. For the same net charge density, a larger radius would result in a reduced number of escaping electrons. For a radius R and positive charge density ρ , the potential for a charged sphere at distance r from its center is⁸

$$\phi(r) = \frac{\rho}{2\epsilon_0} \left(R^2 - \frac{r^2}{3} \right). \quad (15)$$

A free electron will escape if its kinetic energy is larger than the potential from the sphere at the boundary $r = R$. Thus, we get the following condition:

$$E_{kin} > \frac{\rho R^2}{2r\epsilon_0}. \quad (16)$$

In the first 1–3 fs in the CR simulation, the charge density ρ will not be large enough to trap any free electrons. As the net charge will rapidly increase and reach the critical potential in this time scale,

it allows for the approximation that the low number of escaping electrons does not affect the results.

C. Coherent scattering calculations

We determined the displacement of the system from the MD simulations weighted by the distribution of the probe pulse and the charge state distribution of the atoms. Given a Gaussian pulse shape⁴⁰ $g(t)$ with duration T , satisfying $\int_0^T g(t)dt = T$, and the time evolution of the fraction of the remaining bound electron in an atom (with atomic number Z) $y(t) = 1 - z/Z$, we determine the weight $w(t)$ as

$$w(t) = \int_t^{t+dt} \left(\frac{g(t)y(t)}{\int_0^T g(t)y(t)dt} \right) dt, \quad (17)$$

where dt is the time step of the MD simulation and T is the total pulse duration. The real space weighting is an approximation of the average probed structure, motivated by the fact that the phases are not well-defined.

In order to compare with the experiment, an observable needs to be computed. We propose that the fragments of the sample could be studied, with, for instance, mass spectrometry or reaction microscopes available at Small Quantum Systems (SQS) at the European XFEL. Alternatively, the signal from coherent scattering in diffraction experiments can be studied. For bulk water, we computed coherent scattering using the structure factor $S(q)$ defined as⁴¹

$$S_{\alpha\beta}(q, t) = 1 + \frac{4\pi\rho_0}{q} \int_0^\infty r(g_{\alpha\beta}(r, t) - 1) \sin(qr) dr, \quad (18)$$

where $g_{\alpha\beta}$ is the radial distribution function (RDF) between atomic species α and β available from the MD simulations. The scattered intensity is then computed numerically as

$$I = \int_0^T g(t) f(q, t)^2 S(q, t) dt, \quad (19)$$

where $f(q, t) = \int \rho(r) e^{iq \cdot r} dr$ is the form-factor defined as the Fourier transform of the atomic electron density at time t and $g(t)$ is the normalized pulse profile. This atomic electron density is computed using the density functional theory calculations in RSPt⁴² for arbitrary electronic configurations. The form-factor f_α for atomic species α at time t is weighted by the all the different electronic configurations j with weight w_j and form-factor f_j as

$$f_\alpha(q, t) = \frac{\sum_j w_{\alpha j}(t) f_{\alpha j}(t)}{\sum_j w_{\alpha j}(t)}, \quad (20)$$

where the weights are extracted from the CR calculations.

III. RESULTS: MODEL VALIDATION AND COMPARISON TO EXPERIMENTAL DATA

A. Non-thermal heating of bulk water

We begin by studying non-thermal heating of water initiated by an XFEL. This is motivated by the previous experiments on non-thermal heating and scattering of water performed at the Linac Coherent Light Source (LCLS).⁴³ The work also included damage

MD simulations, which were then matched to the CR results instead of directly coupling these, did not treat free electron shielding, and did not dynamically adjust bond parameters. In this work, we used the same Protein Data Bank (PDB) structure for the water and CR calculations but now instead used our updated hybrid CR/MD model to simulate non-thermal heating and scattering.

Two pulses with a flat temporal profile and 6860 eV photon energy were used in our simulations. One with a 25 fs pulse duration and an intensity of $7 \times 10^{18} \text{ W cm}^{-2}$, and another with a 75 fs pulse duration and an intensity of $4.5 \times 10^{18} \text{ W cm}^{-2}$. The real-space dynamics of the atoms is shown in the radial distribution function in Fig. 2. We can see that the x-ray pulse alters the structure of water by increasing the disorder of the system. This is noted by the uniform distribution of the RDF at the end of the simulations, compared to the native structure of water at 0 fs (for reference, the RDF for un-ionized water is shown in the original experimental work.⁴³) In the simulations, we alter the LJ parameters based on the reduction of bound electrons (net-charge). The ionic radius is, therefore, reduced and the atoms can come closer to each other compared to the native oxygen–oxygen RDF shown in Fig. 3 of Beyerlein *et al.*⁴³ For the 25 fs

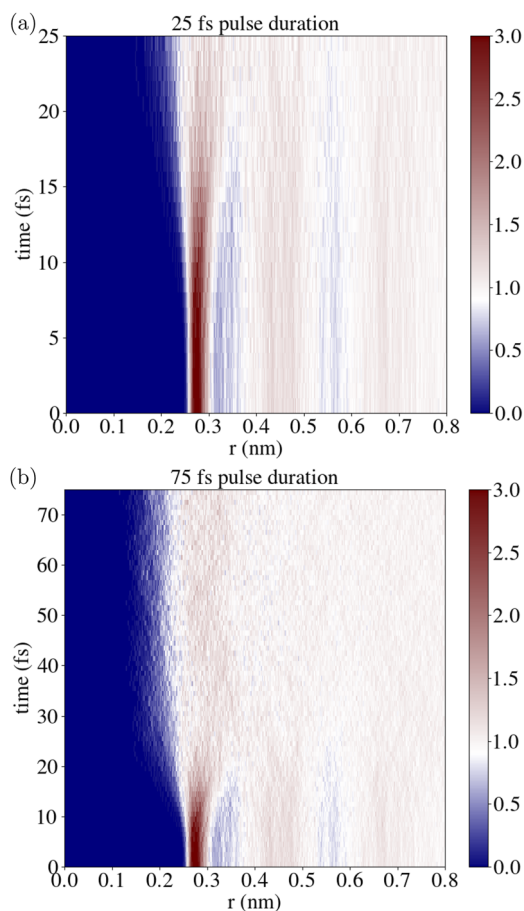


FIG. 2. Oxygen–oxygen RDF for bulk water and pulse duration of (a) 25 fs with intensity $7 \times 10^{18} \text{ W cm}^{-2}$ and (b) 75 fs with intensity $4.5 \times 10^{18} \text{ W cm}^{-2}$.

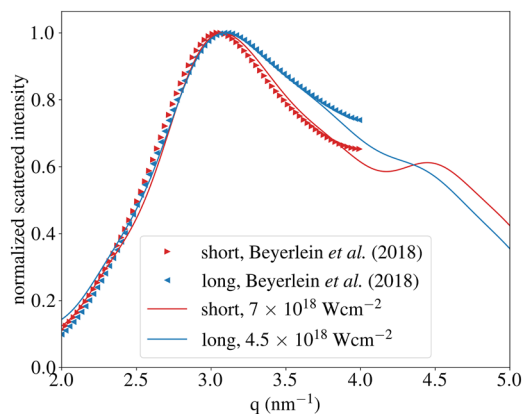


FIG. 3. Scattering of bulk water using the newly developed model compared to experimental data.⁴³ The red curve is the short 25 fs pulse, with intensity 7×10^{18} W cm^{-2} and the blue is 75 fs long with an intensity of 4.5×10^{18} W cm^{-2} .

pulse, disorder starts to be significant after roughly 15 fs and photons scatter-off, to a large extent from a near native structure. For the 75 fs pulse, disorder is introduced around 20 fs, and the pulse largely scatters from a sample that is far from its native structure. This makes the total scattered intensity significantly different compared to the signal from native bulk water. We note that the time scale of the disorder for both pulses (15 and 20 fs, respectively) corresponds to when the sample has been exposed to a similar fluence of $\sim 10^5$ J/cm^2 (15 fs 7×10^{18} W cm^{-2} and 20 fs 4.5×10^{18} W cm^{-2} , respectively).

Using Eq. (19), we calculate the scattered intensity from bulk water as it is probed by the XFEL and contrast it with the experimental results shown in Fig. 3. The simulations provide the first and

second peak in the scattered intensity, encoding the frequency of the relative distance between O–O coordination peaks. In order to reproduce the scattering curves in the experimental data using our model, it is necessary to decrease the fluence relative to the values documented in the referenced paper. We also need to reduce the ratio between the intensities of the long and short pulses. The intensity in XFEL experiments can vary substantially between shot-to-shot and the fluence in the original study is an average one. Both the spatial and temporal distributions of the intensity can vary within a shot, making it difficult to accurately determine the fluence that the sample is exposed to. In Fig. 4, we show a range of different x-ray intensities to understand how increasing the incident intensity leads to changes in the structure and scattering signal. Studying structural changes in water for a range of x-ray intensities that are relevant at XFELs is motivated by its abundance in biological systems and its use in delivering protein crystals in SFX. We cover the same intensity range for the two pulse durations and this corresponds to different fluences, which are shown side by side in Fig. 4(a). It is shown in Fig. 4(a) that as one increases the x-ray intensity, the momentum transfer values above ~ 3.5 nm^{-1} start to accumulate scattering intensity. This means that the structure is changing, where new length scales are occupied by the oxygen atoms. In Fig. 4(b), we show the average ionization with increasing fluence reached by oxygen atoms when the x-ray pulse peaks and ends. The ionization states of the oxygen are similar for both pulse durations at the same fluence. The results demonstrate that changes in the scattering intensity for similar fluences are largely owed to structural changes during the pulse duration.

B. Disulfide bond breaking in femtosecond crystallography with x-ray pump-probe

In the second case study, we simulate an SFX x-ray experiment from Nass *et al.*,⁵ where a pump (photon energy above iron

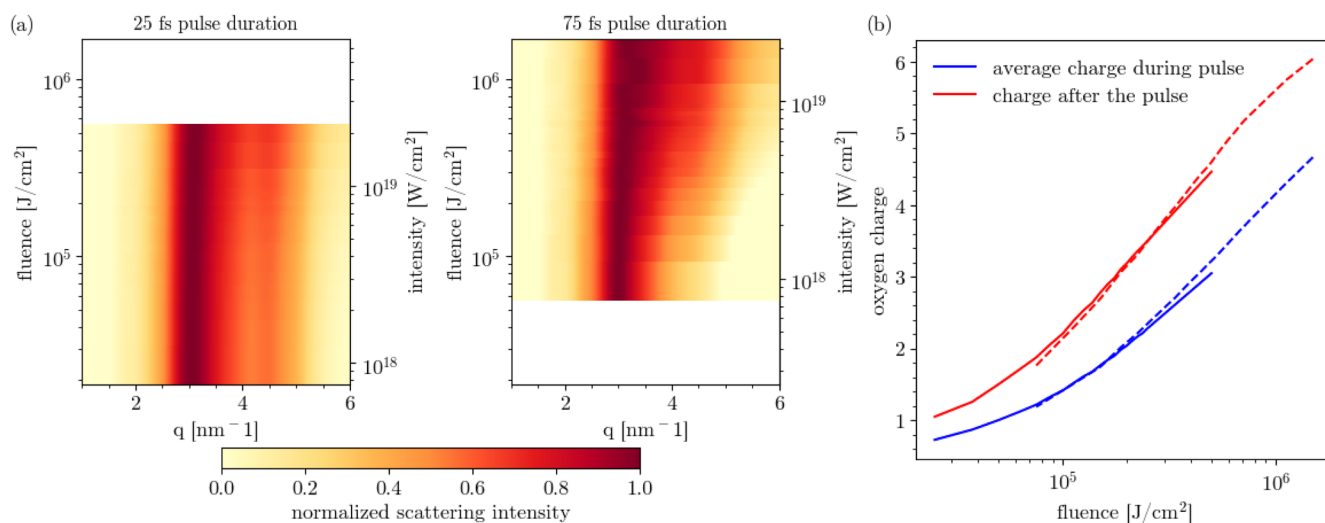


FIG. 4. (a) Time-integrated scattering as a function of momentum transfer and the incident XFEL intensity for the 25 and 75 fs pulse duration, shown both as a function of fluence (left axis) and intensity (right axis). Note that for the same intensity, the fluence of the long pulse is a factor three times higher than for the short pulse. (b) Oxygen charge averaged over the pulse duration (in blue) and after the pulse (in red). The solid and dashed lines represent results for the 25 and 75 fs pulse durations, respectively.

K-edge) triggered ionization effects that were probed (photon energy below iron K-edge) at various time delays in the range 0–110 fs. We focus uniquely on the results presented for disulfide (S–S) bond lengths from a lysozyme target. Both the x-ray pulses were reported to have comparable fluences and 15 fs duration. Although the experimental intensity is estimated at $I_0 = 5.3 \times 10^{19} \text{ W cm}^{-2}$ split equally between the two pulses, the accompanying simulations demonstrate best agreement with 13% of I_0 . The reported findings open interesting questions about the exact illumination on the sample and the modeling considerations that might be relevant for reproducing experimental data.

We solvated a hen egg-white lysozyme unit-cell (PDB 1HEW) containing eight asymmetric units (25 072 atoms in total) and followed the evolution of the disulfide bonds in the Cystine amino-acids with CR/MD simulations. We model both the pump and probe temporal profiles as a Gaussian with 15 fs FWHM. We simulated various probe delays at two different x-ray intensities. We fixed the photon energy of the pump and probe at 7152 and 7072 eV, respectively. The experimental and our simulated pulse-averaged S–S bond distances are compared and shown in Fig. 5.

The highest intensity that we explored ($1 \times 10^{19} \text{ W cm}^{-2}$ for each x-ray pulse) shows good agreement with the experimental data for probe delays of 40 fs or greater. For shorter delays, our simulations required a lower fluence of $3.5 \times 10^{18} \text{ W cm}^{-2}$ (roughly 60% decrease) for each pulse to match to the experiment. For both the intensities we considered, the S–S displacement reaches saturation with higher probe times, which is attributed to the ion caging effect where neighboring atoms provide a force that limits the bond's expansion.⁵ The discrepancy of the experimental data points near 40 fs could suggest short pulse delays correlate to low fluence in the focus compared to the measurements carried out at longer time delays. In Fig. 6, we compare the average ionization of the atoms at 40 fs delay for the two intensities.

Our simulated intensities deviate by roughly a factor of two from experimental values, showing a better agreement compared

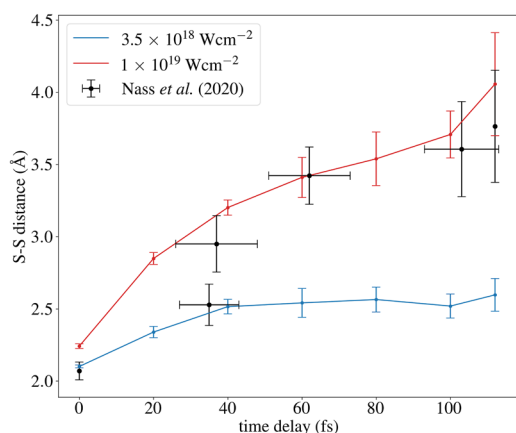


FIG. 5. Pulse weighted relative displacement between the disulfide bond (S–S) as a function of probe delay. The data are averaged over all disulfide bonds in the unit cell. Nass *et al.*⁵ represent the experimental data. The legend shows the intensity for each x-ray pulse, pump, and probe.

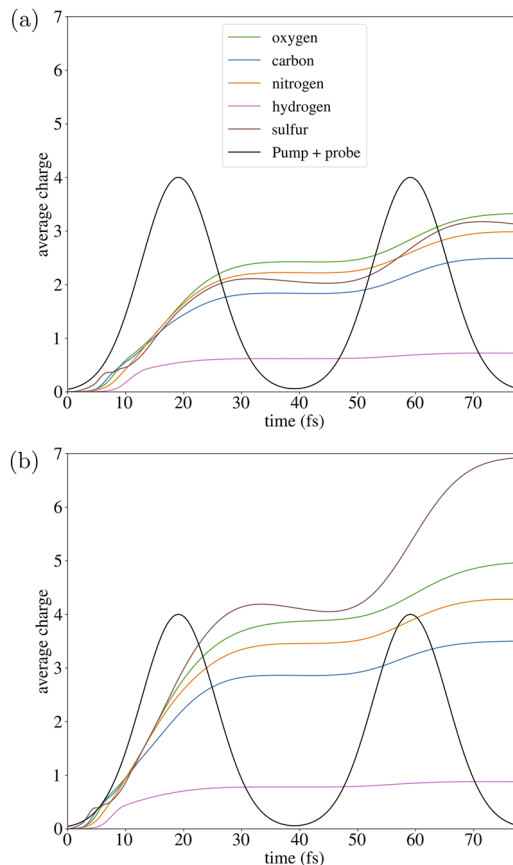


FIG. 6. Average charge of atoms in the lysozyme crystal as a function of delay for intensities of (a) 3.5×10^{18} and (b) $1.0 \times 10^{19} \text{ W cm}^{-2}$.

to the theoretical calculations presented in Nass *et al.*⁵ The most notable addition to our simulations is the inclusion of bonded interactions through Morse potentials. Volume integration could also account for some discrepancies. Assuming a spatial Gaussian profile with a $0.2 \mu\text{m}$ focus at FWHM and a sample size of $0.5 \mu\text{m}$, we estimate, in the most extreme cases, the crystal is exposed to non-uniform illumination with a variance of $<15\%$.

In both simulations and experiments, we see that there should be some correlated motion, which is understood from the relatively small variance for short delays compared to the longer delays. Thus, the variance will put a limit on the achievable resolution. Therefore, using our model, we provide estimations of the maximum attainable resolution.

IV. RESULTS: APPLICATION OF THE MODEL AND PREDICTIONS

A. Fragmentation dynamics of a methane cluster

In this scenario, we investigate the radiation damage during an XFEL single particle imaging experiment on a methane cluster consisting of $\sim 45 \text{ k}$ atoms, which serves as a model system for biological macromolecules, such as proteins and viruses. Previous experiments have been done on fragmentation dynamics in

methane clusters,⁴⁴ and recently, there has been an increased interest in coherent imaging of nano-clusters that turn into plasma.⁴⁵ To study the cluster's damage evolution, we envision an x-ray pump-probe scheme of delays ranging 0–100 fs with an intensity of 10^{19} W cm⁻² and 8 keV photon energy with a 15 fs duration flat-top temporal profile. We constructed a non-crystalline cluster by placing atoms randomly over a spherical volume limited by their van der Waals radii to match a density of 0.4 g/cm³. Later, we minimized the structure using the steepest descent. To describe bonded interactions, we used Morse potentials and a harmonic angle term. The parameters for the potentials were extracted from the Optimized Potentials for Liquid Simulations - all atoms (OPLS-AA) forcefield.^{46,47}

During exposure, we expect surface atoms to experience a different electrostatic environment compared to those located deeper

in the cluster.^{8,48} In addition, atoms at the surface are less affected by collisional events and have a higher probability of moving into vacuum due to the reduced number of neighbors. For a small cluster, the ratio of the number of core to surface atoms is small. Assuming a screened Coulomb potential dictates the interaction of the entire cluster is not an appropriate approximation since surface atoms are less screened. For a bigger system, where the ratio of the number of core atoms to surface atoms is large, the dynamics is dominated by the screened potentials. CR simulations assume all free-electrons remain trapped inside the environment, which constrains the smallest cluster size that we can consider to keep this assumption valid. To address this question, we begin by studying the resulting cluster charge for various probe delays, shown in Fig. 7(a). Based on these observations, in Fig. 7(b), we calculate the electrostatic potential expected from a charged sphere using Eq. (16) from

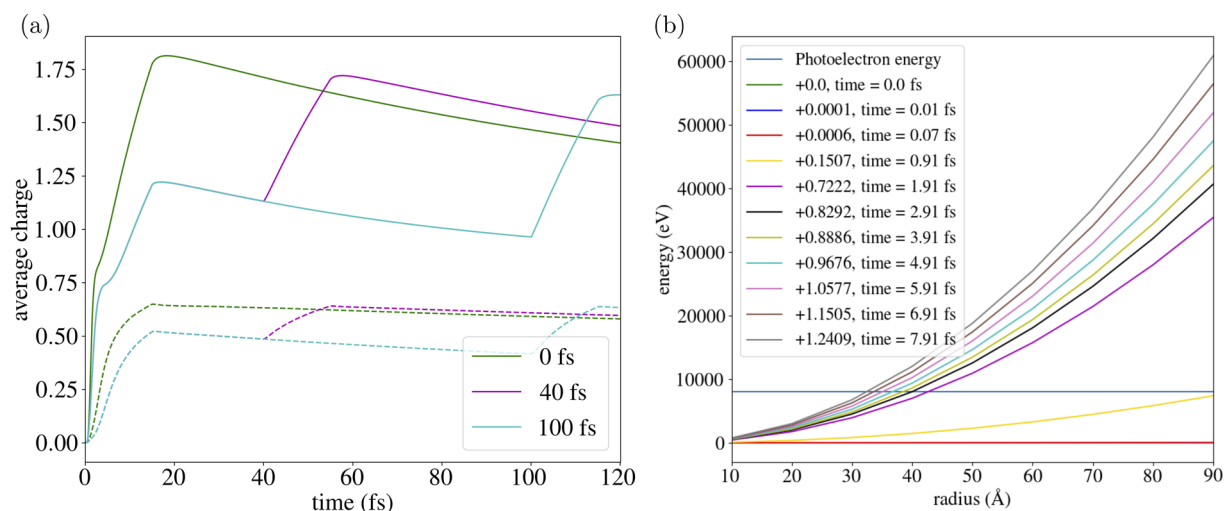


FIG. 7. Collisional radiative simulation results for a methane cluster exposed to 8 keV photon energy, 10^{19} W cm⁻² intensity, and 15 fs FWHM duration x-ray pump-probe pulses. (a) Average hydrogen and carbon charge at three different time delays (0, 40, and 100 fs). (b) Comparing the photoelectron energy (horizontal line) to the time-evolution of the cluster's electrostatic buildup based on the ionizations predicted on the 0 fs delay-case, assuming all photoionized electrons escape.

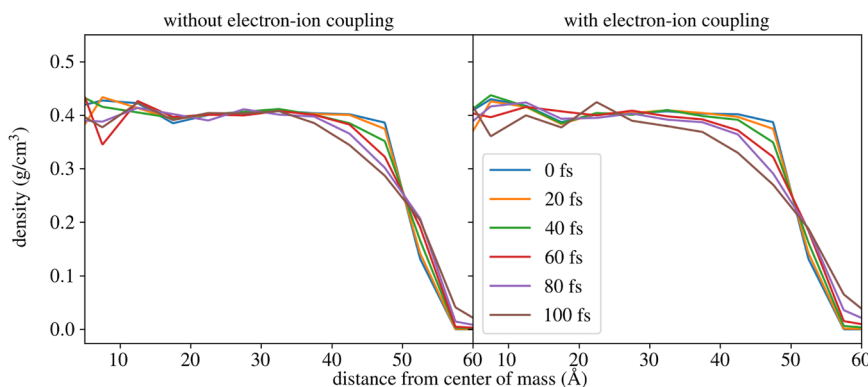


FIG. 8. Mass density including hydrogen and carbon of a 5.5 nm methane cluster as a function of distance, probe delay, and distance from the center of mass. The density for each probe delay is averaged during the probe-pulse duration. A resolution of 5 Å was used to sample the radius of the sphere. The left figure corresponds to a simulation without electron-ion coupling, and the right figure is with electron-ion coupling.

the time-evolving ionization assuming electrons escape and compare to the kinetic energy from primary photo-ejected electrons. We conclude that a cluster with a radius of 5.5 nm builds up enough electrostatic potential energy to trap photoionized electrons within 2 fs of the x-ray pump and probe.

To investigate x-ray-induced damage dynamics, we focus on the probe-pulse averaged electron density as a function of distance from its center of mass (COM) shown in Fig. 8, and we contrast the results with and without electron-ion coupling. As time evolves, more outer layers of the cluster are removed indicated by the reduction in the density close to the surface and occupation of larger distances from COM than the initial radius of the cluster. The density is largely intact up to the 100 fs probe delay. We conclude that the effect of the electron-ion coupling using a resolution of 5 Å provides a negligible difference. We further investigated the different fragments that are produced during the coherent imaging of the system. Fractional ion yields, as shown in Fig. 9, provide information regarding the fragments with which the specific net-charge exist. We again contrast including/excluding electron-ion coupling. At short time scales, the two models are similar for the early probe delays of 0 and 20 fs probe delays, but they deviate at longer delay times. Comparing the 0 and 100 fs time delays, the ion yield are significantly different but exhibit similar densities at the computed resolution of 5 Å.

B. Discussion on the effect of electron-ion coupling on SPI and SFX

The breakup of a sample exposed to x-ray radiation encodes structural information that can be captured from trajectories, kinetic energies, and mass over charge ratios. The dynamics of possible fragments or ions depends on the structure and the deposition of energy from the x-ray pulse. In our MD model, the latter is mediated via three main channels: (1) changes to the ionization levels of the atoms, (2) free electrons included in an implicit way to screen electrostatic and non-bonded interactions, and (3) ion-electron coupling that dictates the energy exchange between these two species. For comparison with fragmentation experiments, it is relevant to assess the effects of the x-ray laser, on short (≤ 100 fs) time scales, and the heating, on picosecond time scales.

We began by studying the effect of including/excluding electron-ion coupling in the damage simulations for the case study on water presented in Sec. III A. For the time scales of interest, which ranged 25–75 fs, the effect of electron-ion coupling did not yield significant differences in the dynamics (data not shown). We explored a second case presented in Sec. IV A related to the ion yield from a methane cluster at various probe time delays. These results are presented in Fig. 9.

For higher intensities, the distribution of ion yield starts to differ earlier. The change in ion yield for the simulation without electron-ion coupling saturates shortly after pulse, where the rate of change is small. However, with coupling the distribution continuously changes. This is because after the pulse has terminated, the simulation without coupling will not be pumped with energy any more, while in the other case, electrons will continue to transfer their kinetic energy to ions. This enables the creation of new mass/charge fragments through the ions having higher kinetic energies since the charge states change very slowly after the pulse.

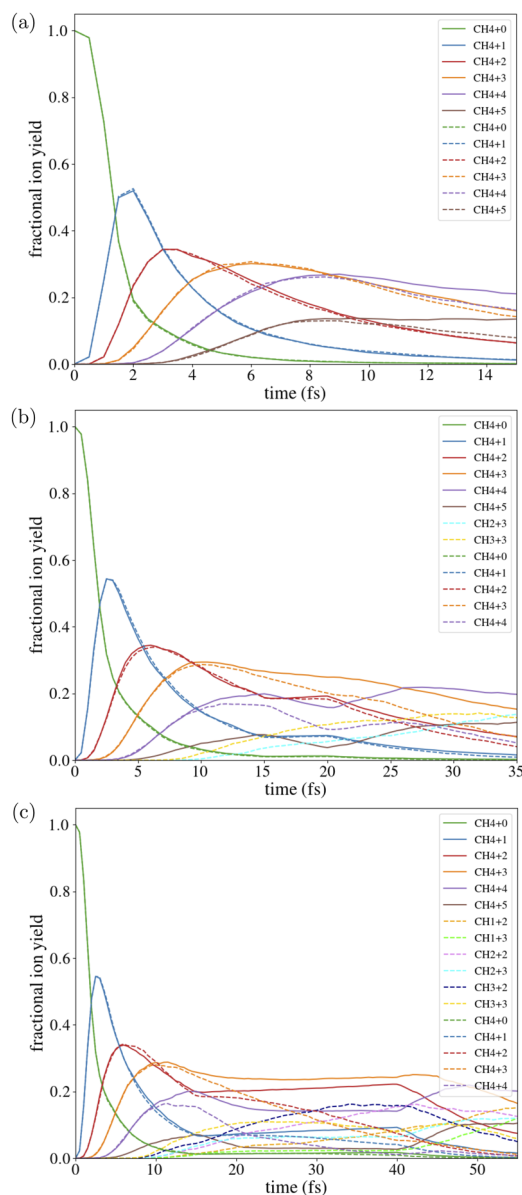


FIG. 9. Difference in the resulting fractional ion yield in a methane cluster due to a 15 fs XFEL pump pulse with XFEL probe delays 0 fs in (a), 20 fs in (b), and 40 fs in (c). The solid lines correspond to simulations with electron-ion coupling, and the dotted lines are without electron-ion coupling.

We conclude for a 15 fs pulse that the dynamics in the sample, as detected in an SPI experiment on a photon detector through coherent diffraction, is not much affected by the mechanisms modeled through the electron-ion coupling. The pulse has the largest effect on the dynamics through the change of charge states and the free electron distribution. Even though electron-ion coupling does not affect time scales relevant for coherent imaging with x-ray laser, the thermodynamics of the system in the MD simulation will not reproduce the CR ones if the coupling

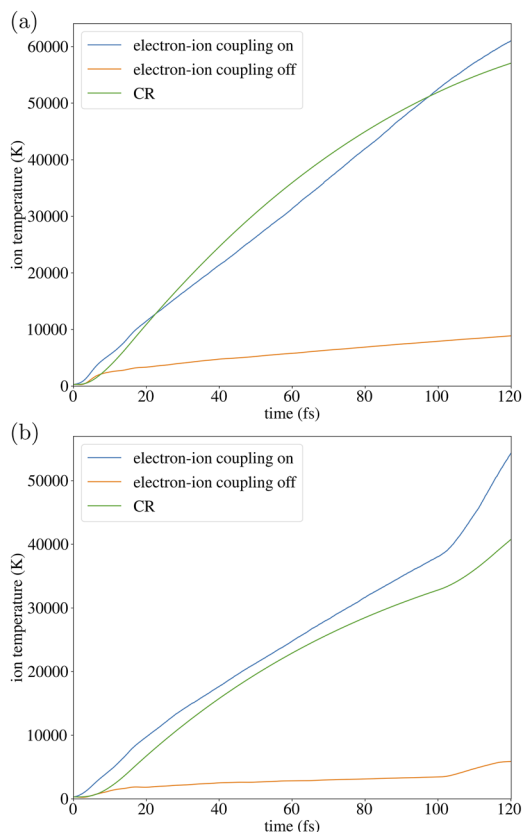


FIG. 10. Ion temperature for the methane cluster given by the CR simulation for (a) 0 fs probe delay and (b) 100 fs delay.

is omitted. We calculated the ion temperature as given by the CR calculations and MD using with and without electron–ion coupling, as shown in Fig. 10. The MD contains hybrid screening as developed in the theory section and charge states from the CR data. We conclude that including electron–ion coupling provides much better agreement with the CR simulations. It is clear that for long time scales, on the order of picoseconds, electron–ion coupling should be included for spherically expanding plasma.

V. CONCLUSION AND OUTLOOK

We have presented a method (MOLDSTRUCT) to compute photon–matter interaction for x-ray lasers, implemented in the classical MD code GROMACS with an addition of collisional-radiative calculations that take into account dynamical changes in the ion and electron dynamics. The method is able to simulate a great variety of samples in different conditions that are explored using high-intensity x-ray lasers. We have compared our theoretical method to two experiments, on bulk water and protein crystals, and we see a quantitatively good agreement. Therefore, we believe that the code will be important in order to assess the limits of experiments and to understand if experiments with sensitive samples have been affected

by radiation damage. It is particularly important to assess structural changes due to damage in time-resolved experiments, since these changes might be interpreted as biological function. The code is presently being used to compare theoretical results to several SFX experiments.

We envision that the model could be directly compared to an experiment where a small molecule crystal⁴⁹ is studied using an x-ray pump–probe scheme at an XFEL. By having a sample containing heavier atoms, which scatter strongly, the atomic movement can be followed as a function of probe delay by analyzing the scattering data using Patterson functions.⁵⁰ The Patterson function is a real space quantity, which is possible to extract from both experiment and the model presented here.

The strengths of the model are that we can access long time scales in large-scale samples. We use a continuum model for electrons, which allows the simulated time steps to be about 10× longer compared to the models following explicit electrons, thus providing a computational gain. We are able to include processes such as electron–ion coupling and also dynamically modify forces with screening and changes in the ionization. The model allows the study of local damage, which is important for protein radiation-damage sensitive parts, such as in metalloproteins. One limitation of the model is that it treats electrons as a gas that instantly thermalizes and does not follow the explicit dynamics of the electrons. Furthermore, our continuous electron model starts with the assumption of a homogeneous distribution and modulates the local interactions between charges with global factors. Any unisotropy atomic dynamics or local effects that would occur in this model will only be dictated by the geometry of the system and local atomic structure. The fast electron dynamics can be modeled with Monte Carlo methods, while the thermal electrons could still be modeled as a gas.⁵¹ Another limitation of the presented model is that it is currently suitable for large samples, which can be described by a plasma phase, where the electrons are trapped and lead to a non-thermal heating of the sample. For simulating small systems, such as small proteins, we are developing a hybrid Monte Carlo/molecular dynamics model, which is applicable for modeling amino acids and proteins.

ACKNOWLEDGMENTS

We thank Erik Marklund, Filipe Maia, and Olof Jönsson and acknowledge the Biophysics Network at the Uppsala University for fruitful discussions. All calculations were performed on the Davinci computer cluster provided by the Laboratory of Molecular Biophysics, Uppsala University. We acknowledge the Project Grants from the Swedish Research Council (Grant Nos. 2018-00740 and 2019-03935), the Röntgen-Ångström Cluster provided by the Swedish Research Council (Grant No. 2021-05988), and the Helmholtz Association through the Center for Free-Electron Laser Science at DESY.

AUTHOR DECLARATIONS

Conflict of Interest

The authors have no conflicts to disclose.

Author Contributions

Ibrahim Dawod: Investigation (equal); Methodology (equal); Software (equal); Validation (equal); Writing – original draft (equal); Writing – review & editing (equal). **Sebastian Cardoch:** Software (equal); Validation (equal); Writing – review & editing (equal). **Tomas André:** Software (equal); Validation (equal); Writing – review & editing (equal). **Emiliano De Santis:** Software (equal); Validation (equal); Writing – review & editing (equal). **Juncheng E:** Software (equal); Validation (equal); Writing – review & editing (equal). **Adrian P. Mancuso:** Conceptualization (equal); Funding acquisition (equal); Resources (equal); Supervision (equal); Writing – original draft (equal); Writing – review & editing (equal). **Carl Coleman:** Conceptualization (equal); Funding acquisition (equal); Investigation (equal); Methodology (equal); Supervision (equal); Writing – original draft (equal); Writing – review & editing (equal). **Nicuser Timneanu:** Conceptualization (equal); Funding acquisition (equal); Investigation (equal); Methodology (equal); Supervision (equal); Writing – original draft (equal); Writing – review & editing (equal).

DATA AVAILABILITY

The data that support the findings of this study are available from the corresponding author upon reasonable request.

REFERENCES

- 1 A. Wlodawer, W. Minor, Z. Dauter, and M. Jaskolski, “Protein crystallography for aspiring crystallographers or how to avoid pitfalls and traps in macromolecular structure determination,” *FEBS J.* **280**, 5705–5736 (2013).
- 2 Y. Cheng, N. Grigorieff, P. A. Penczek, and T. Walz, “A primer to single-particle cryo-electron microscopy,” *Cell* **161**, 438–449 (2015).
- 3 J. Frank, “Time-resolved cryo-electron microscopy: Recent progress,” *J. Struct. Biol.* **200**, 303–306 (2017).
- 4 A. P. Mancuso, A. Aquila, L. Batchelor, R. J. Bean, J. Bielecki, G. Borchers, K. Doerner, K. Giewekemeyer, R. Graceffa, O. D. Kelsey *et al.*, “The single particles, clusters and biomolecules and serial femtosecond crystallography instrument of the European XFEL: Initial installation,” *J. Synchrotron Radiat.* **26**, 660–676 (2019).
- 5 K. Nass, A. Gorel, M. M. Abdullah, A. V. Martin, M. Kloos, A. Marinelli, A. Aquila, T. R. Barends, F.-J. Decker, R. Bruce Doak *et al.*, “Structural dynamics in proteins induced by and probed with X-ray free-electron laser pulses,” *Nat. Commun.* **11**, 1814 (2020).
- 6 N.-E. Christou, V. Apostolopoulou, D. V. Melo, M. Ruppert, A. Fadini, A. Henkel, J. Sprenger, D. Oberthuer, S. Günther, A. Pateras *et al.*, “Time-resolved crystallography captures light-driven DNA repair,” *Science* **382**, 1015–1020 (2023).
- 7 R. Neutze, R. Wouts, D. Van der Spoel, E. Weckert, and J. Hajdu, “Potential for biomolecular imaging with femtosecond X-ray pulses,” *Nature* **406**, 752–757 (2000).
- 8 S. P. Hau-Riege, R. A. London, and A. Szoke, “Dynamics of biological molecules irradiated by short x-ray pulses,” *Phys. Rev. E* **69**, 051906 (2004).
- 9 C. H. Yoon, M. V. Yurkov, E. A. Schneidmiller, L. Samoylova, A. Buzmakov, Z. Jurek, B. Ziaja, R. Santra, N. D. Loh, T. Tschentscher, and A. P. Mancuso, “A comprehensive simulation framework for imaging single particles and biomolecules at the European X-ray free-electron laser,” *Sci. Rep.* **6**, 24791 (2016).
- 10 A. V. Martin, J. K. Corso, C. Coleman, N. Timneanu, and H. M. Quiney, “Single-molecule imaging with longer X-ray laser pulses,” *IUCr* **2**, 661–674 (2015).
- 11 H. N. Chapman, P. Fromme, A. Barty, T. A. White, R. A. Kirian, A. Aquila, M. S. Hunter, J. Schulz, D. P. DePonte, U. Weierstall *et al.*, “Femtosecond X-ray protein nanocrystallography,” *Nature* **470**, 73–77 (2011).
- 12 C. Östlin, N. Timneanu, C. Coleman, and A. V. Martin, “Is radiation damage the limiting factor in high-resolution single particle imaging with X-ray free electron lasers?,” *Struct. Dyn.* **6**, 044103 (2019).
- 13 Y. Hirano, K. Takeda, and K. Miki, “Charge-density analysis of an iron–sulfur protein at an ultra-high resolution of 0.48 Å,” *Nature* **534**, 281–284 (2016).
- 14 K. Pande, J. Donatelli, E. Malmerberg, L. Foucar, C. Bostedt, I. Schlichting, and P. Zwart, “Ab initio structure determination from experimental fluctuation x-ray scattering data,” *Proc. Natl. Acad. Sci. U. S. A.* **115**, 11772 (2018).
- 15 P. J. Ho, C. Knight, and L. Young, “Fluorescence intensity correlation imaging with high spatial resolution and elemental contrast using intense x-ray pulses,” *Struct. Dyn.* **8**, 044101 (2021).
- 16 U. Zastra, S. Göde, and M. Nakatsutsumi, “How x-ray free electron lasers enable ultrafast dynamics studies in high-energy-density science,” *Synchrotron Radiat. News* **29**, 24–29 (2016).
- 17 J. L. Dickerson, P. T. N. McCubbin, and E. F. Garman, “RADDOSE-XFEL: Femtosecond time-resolved dose estimates for macromolecular X-ray free-electron laser experiments,” *J. Appl. Crystallogr.* **53**, 549–560 (2020).
- 18 F. R. Graziani, V. S. Batista, L. X. Benedict, J. I. Castor, H. Chen, S. N. Chen, C. A. Fichtl, J. N. Glosli, P. E. Grabowski, A. T. Graf, S. P. Hau-Riege, A. U. Hazi, S. A. Khairallah, L. Krauss, A. B. Langdon, R. A. London, A. Markmann, M. S. Murillo, D. F. Richards, H. A. Scott, R. Shepherd, L. G. Stanton, F. H. Streitz, M. P. Surh, J. C. Weisheit, and H. D. Whitley, “Large-scale molecular dynamics simulations of dense plasmas: The Cimarron project,” *High Energy Density Phys.* **8**, 105–131 (2012).
- 19 Z. Jurek, S.-K. Son, B. Ziaja, and R. Santra, “XMDYN and XATOM: Versatile simulation tools for quantitative modeling of X-ray free-electron laser induced dynamics of matter,” *J. Appl. Crystallogr.* **49**, 1048–1056 (2016).
- 20 P. J. Ho and C. Knight, “Large-scale atomistic calculations of clusters in intense x-ray pulses,” *J. Phys. B: At., Mol. Opt. Phys.* **50**, 104003 (2017).
- 21 A. Kozlov, A. V. Martin, and H. M. Quiney, “Hybrid plasma/molecular-dynamics approach for efficient XFEL radiation damage simulations,” *Crystals* **10**, 478 (2020).
- 22 M. Bergh, N. Timneanu, and D. van der Spoel, “Model for the dynamics of a water cluster in an x-ray free electron laser beam,” *Phys. Rev. E* **70**, 051904 (2004).
- 23 B. Ziaja, V. Saxena, S.-K. Son, N. Medvedev, B. Barbrel, B. Woloncewicz, and M. Stransky, “Kinetic Boltzmann approach adapted for modeling highly ionized matter created by x-ray irradiation of a solid,” *Phys. Rev. E* **93**, 053210 (2016).
- 24 V. Saxena and B. Ziaja, “Hydrodynamic model for expansion and collisional relaxation of x-ray laser-excited multi-component nanoplasma,” *Phys. Plasmas* **23**, 012710 (2016).
- 25 MolDStruct builds on “GROMACS” and is available at <https://github.com/moldstruct/cr-md>.
- 26 H. A. Scott and R. W. Mayle, “GLF—A simulation code for X-ray lasers,” *Appl. Phys. B* **58**, 35–43 (1994).
- 27 S. Pronk, S. Páll, R. Schulz, P. Larsson, P. Bjelkmar, R. Apostolov, M. R. Shirts, J. C. Smith, P. M. Kasson, D. van der Spoel, B. Hess, and E. Lindahl, “GROMACS 4.5: A high-throughput and highly parallel open source molecular simulation toolkit,” *Bioinformatics* **29**, 845–854 (2013).
- 28 B. Hess, C. Kutzner, D. van der Spoel, and E. Lindahl, “GROMACS 4: Algorithms for highly efficient, load-balanced, and scalable molecular simulation,” *J. Chem. Theory Comput.* **4**, 435–447 (2008).
- 29 J. C. Stewart and K. D. Pyatt, Jr., “Lowering of ionization potentials in plasmas,” *Astrophys. J.* **144**, 1203 (1966).
- 30 R. M. More, “Electronic energy-levels in dense plasmas,” *J. Quant. Spectrosc. Radiat. Transfer* **27**, 345–357 (1982).
- 31 S. Cardoch, F. Trost, H. A. Scott, H. N. Chapman, C. Coleman, and N. Timneanu, “Decreasing ultrafast x-ray pulse durations with saturable absorption and resonant transitions,” *Phys. Rev. E* **107**, 015205 (2023).
- 32 J. Andreasson, B. Iwan, A. Andrejczuk, E. Abreu, M. Bergh, C. Coleman, A. J. Nelson, S. Bajt, J. Chalupsky, H. N. Chapman, R. R. Fäustlin, V. Hajkova, P. A. Heimann, B. Hjörvarsson, L. Juha, D. Klinger, J. Krzywinski, B. Nagler, G. K. Pálsson, W. Singer, M. M. Seibert, R. Sobierajski, S. Toleikis, T. Tschentscher, S. M. Vinko, R. W. Lee, J. Hajdu, and N. Timneanu, “Saturated ablation in metal hydrides and acceleration of protons and deuterons to keV energies with a soft-x-ray laser,” *Phys. Rev. E* **83**, 016403 (2011).

- ³³N. Goga, A. Rzepiela, A. De Vries, S. Marrink, and H. Berendsen, "Efficient algorithms for Langevin and DPD dynamics," *J. Chem. Theory Comput.* **8**, 3637–3649 (2012).
- ³⁴J. M. Molina and T. White, "A molecular dynamics study of laser-excited gold," *Matter Radiat. Extremes* **7**, 036901 (2022).
- ³⁵F. F. Chen *et al.*, *Introduction to Plasma Physics and Controlled Fusion* (Springer, 1984), Vol. 1.
- ³⁶M. S. Murillo and J. C. Weisheit, "Dense plasmas, screened interactions, and atomic ionization," *Phys. Rep.* **302**, 1–65 (1998).
- ³⁷X. Li, F. Rosmej, V. Lisitsa, and V. Astapenko, "An analytical plasma screening potential based on the self-consistent-field ion-sphere model," *Phys. Plasmas* **26**, 033301 (2019).
- ³⁸O. Grånäs, N. Timneanu, I. Eliah Dawod, D. Ragazzon, S. Trygg, P. Souvatzis, T. Edvinsson, and C. Caleman, "Femtosecond bond breaking and charge dynamics in ultracharged amino acids," *J. Chem. Phys.* **151**, 144307 (2019).
- ³⁹E. Apol, R. Apostolov, H. Berendsen, A. Van Buuren, P. Bjelkmar, R. Van Drunen, A. Feenstra, G. Groenhof, P. Kasson, P. Larsson *et al.*, *GROMACS User Manual Version 4.5.4*, Royal Institute of Technology and Uppsala University, Stockholm, 2010.
- ⁴⁰H. O. Jönsson, N. Timneanu, C. Östlin, H. A. Scott, and C. Caleman, "Simulations of radiation damage as a function of the temporal pulse profile in femtosecond X-ray protein crystallography," *J. Synchrotron Radiat.* **22**, 256–266 (2015).
- ⁴¹A. Soper, "Joint structure refinement of x-ray and neutron diffraction data on disordered materials: Application to liquid water," *J. Phys.: Condens. Matter* **19**, 335206 (2007).
- ⁴²J. M. Wills, O. Eriksson, P. Andersson, A. Delin, O. Grechnev, M. Alouani, J. M. Wills, M. Alouani, P. Andersson, A. Delin *et al.*, "The full-potential electronic structure problem and RSPt," in *Full-Potential Electronic Structure Method: Energy and Force Calculations with Density Functional and Dynamical Mean Field Theory* (Springer Nature, 2010), pp. 47–73.
- ⁴³K. R. Beyerlein, H. O. Jönsson, R. Alonso-Mori, A. Aquila, S. Bajt, A. Barty, R. Bean, J. E. Koglin, M. Messerschmidt, D. Ragazzon *et al.*, "Ultrafast nonthermal heating of water initiated by an x-ray free-electron laser," *Proc. Natl. Acad. Sci. U. S. A.* **115**, 5652–5657 (2018).
- ⁴⁴B. Iwan, J. Andreasson, M. Bergh, S. Schorb, H. Thomas, D. Rupp, T. Gorkhovev, M. Adolph, T. Möller, C. Bostedt, J. Hajdu, and N. Timneanu, "Explosion, ion acceleration, and molecular fragmentation of methane clusters in the pulsed beam of a free-electron laser," *Phys. Rev. A* **86**, 033201 (2012).
- ⁴⁵D. Rupp, L. Flückiger, M. Adolph, A. Colombo, T. Gorkhovev, M. Harmand, M. Krikunova, J. P. Müller, T. Oelze, Y. Ovcharenko, M. Richter, M. Sauppe, S. Schorb, R. Treusch, D. Wolter, C. Bostedt, and T. Möller, "Imaging plasma formation in isolated nanoparticles with ultrafast resonant scattering," *Struct. Dyn.* **7**, 034303 (2020).
- ⁴⁶W. L. Jorgensen, D. S. Maxwell, and J. Tirado-Rives, "Development and testing of the OPLS all-atom force field on conformational energetics and properties of organic liquids," *J. Am. Chem. Soc.* **118**, 11225–11236 (1996).
- ⁴⁷G. A. Kaminski, R. A. Friesner, J. Tirado-Rives, and W. L. Jorgensen, "Evaluation and reparametrization of the OPLS-AA force field for proteins via comparison with accurate quantum chemical calculations on peptides," *J. Phys. Chem. B* **105**, 6474–6487 (2001).
- ⁴⁸P. J. Ho, B. J. Daurer, M. F. Hantke, J. Bielecki, A. Al Haddad, M. Bucher, G. Doumy, K. R. Ferguson, L. Flückiger, T. Gorkhovev, B. Iwan, C. Knight, S. Moeller, T. Osipov, D. Ray, S. H. Southworth, M. Svenda, N. Timneanu, A. Ulmer, P. Walter, J. Hajdu, L. Young, F. R. N. C. Maia, and C. Bostedt, "The role of transient resonances for ultra-fast imaging of single sucrose nanoclusters," *Nat. Commun.* **11**, 167 (2020).
- ⁴⁹E. A. Schriber, D. W. Paley, R. Bolotovskiy, D. J. Rosenberg, R. G. Sierra, A. Aquila, D. Mendez, F. Poitevin, J. P. Blaschke, A. Bhowmick *et al.*, "Chemical crystallography by serial femtosecond X-ray diffraction," *Nature* **601**, 360–365 (2022).
- ⁵⁰B. Rupp, *Biomolecular Crystallography: Principles, Practice, and Application to Structural Biology* (Garland Science, 2009).
- ⁵¹N. Medvedev, "XTANT-3: X-ray-induced thermal and nonthermal transitions in matter: Theory, numerical details, user manual," [arXiv:2307.03953](https://arxiv.org/abs/2307.03953) [cond-mat.other] (2023).